Speed Gain in Elastic Joint Robots: An Energy Conversion-Based Approach

Nico Mansfeld, Manuel Keppler, and Sami Haddadin

***Abstract*—Like humans or animals, robots with compliant joints are capable of performing explosive or cyclic motions by making systematic use of energy storage and release, and it has been shown that they can outperform their rigid counterparts in terms of peak velocity. For rigid joint robots, there exist well-established, computationally inexpensive tools to compute the maximum achievable Cartesian endpoint velocity, which is an important performance and safety characteristic for robot designs. For elastic joint robots, optimal control is usually employed to determine the maximum possible link velocity together with the associated trajectory, which is time consuming and computationally costly for most systems. In this letter, we propose methods to obtain estimates of the maximum achievable Cartesian endpoint velocities of gravity-free elastic joint robots that have computational requirements close to the rigid joint robot case. We formulate an optimal control problem to verify the methods and provide results for a planar 3R robot. Furthermore, we compare the results of our approach with those from real-world throwing experiments which were previously conducted on the elastic DLR David system. Finally, we apply the methods to derive and quantitatively compare the safety properties of DLR David and a hypothetically rigid version of this robot in terms of the Safety Map framework proposed in our previous work.**

***Index Terms*—Compliant joints and mechanisms, methods and tools for robot system design, human-centered robotics, physical human-robot interaction, robot safety.**

I. Introduction

IN RECENT years, many robotic systems with intrinsic joint compliance have been developed, e.g., legged robots, hands, prostheses, manipulators, and humanoids. An overview of the design principles for realizing series elastic and variable impedance actuation is given in [1]. The motivation for deliberately introducing joint elasticity in manipulators is the improvement of mechanical robustness, safety in human-robot interaction, and the inherent capability to store and release energy which can be utilized to outperform rigid robots by means of energy efficiency and peak velocity.

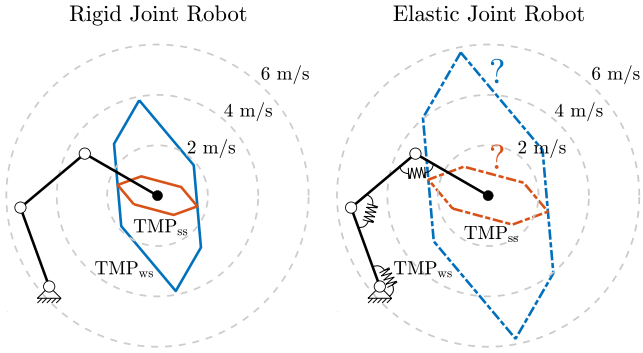

Fig. 1. Achievable Cartesian endpoint velocities of a planar 3R rigid (left) and elastic joint robot (right) for the illustrated configuration. For the rigid joint robot, the achievable velocities are represented by polytopes, where $\mathrm{TMP}_{\mathrm{ws}}$ denotes the weak sense (angular velocity may be non-zero) and $\mathrm{TMP}_{\mathrm{ss}}$ the strong sense (purely translational velocities) polytope. The goal of this letter is to derive the maximum possible endpoint velocities for elastic joint robots, which are known to be capable of achieving higher velocities than their rigid counterparts.

The (configuration-dependent) maximum achievable endpoint velocity is an important characteristic for assessing and optimizing both the performance and safety properties of a robot design. In motion and task planning methods and in the early design phase of robot mechanics where quick iterations are desirable, it is key that the achievable TCP velocities can be estimated with reasonable accuracy and minimal computational effort. For rigid joint robots, the maximum Cartesian tip velocity is given by the so-called translational manipulability polytope (TMP) [2], which depends on the robot kinematics and motor velocity bounds and has little computational requirements; see Fig. 1. For elastic joint robots, analytical solutions to maximum link velocity and (time-optimal) excitation exist for 1-DOF visco-elastic joints [3]–[8]. In [9]–[11], explosive throwing trajectories were generated for systems with two or more DOF using optimal control. Such numerical techniques are typically computationally costly, time consuming, and require accurate modeling of the complex system dynamics. Therefore they are hardly suitable for motion/task planning schemes and the early robot design phase.

In this letter, we propose methods to estimate the configuration-dependent maximum possible endpoint velocities of gravity-free elastic joint robots that take relevant real-world

Manuscript received October 15, 2020; accepted February 21, 2021. Date of publication March 24, 2021; date of current version April 13, 2021. This letter was recommended for publication by Associate Editor J. Zhang and Editor C. Gosselin upon evaluation of the reviewers' comments. This work was supported in part by the European Union's Horizon 2020 Research and Innovation Programme as part of the projects ILIAD (under Grant 732737) and DARKO (under Grant 101017274), and in part by the Lighthouse Initiative Geriatronics by StMWi Bayern (Project X, under Grant 5140951) and LongLeif GaPa gGmbH (Project Y, under Grant 5140953). *(Corresponding author: Nico Mansfeld.)*

Nico Mansfeld and Sami Haddadin are with the Chair of Robotics Science and Systems Intelligence, Munich School of Robotics and Machine Intelligence, Technical University of Munich (TUM), 80797 Munich, Germany (e-mail: nico.mansfeld@tum.de; sami.haddadin@tum.de).

Manuel Keppler is with the Institute of Robotics and Mechatronics, German Aerospace Center (DLR), 82234 Wessling, Germany (e-mail: manuel.keppler@dlr.de).

This letter has supplementary downloadable material available at https://doi.org/10.1109/LRA.2021.3068698, provided by the authors.

Digital Object Identifier 10.1109/LRA.2021.3068698

constraints on motor velocity and spring potential energy into account with computation requirements close to the rigid joint robot case. We make several hypotheses on how and to what extent the motor velocity and the elastic energy can be exploited and converted to link kinetic energy. The hypotheses are exemplified using a 3R planar robot. For verification, we compare the theory with the optimal control solution. Here, we observe a reasonable agreement in terms of maximum achievable TCP velocity and show that the computation time of the proposed methods is orders of magnitude lower than the time required to compute the optimal control trajectories. To further confirm the validity of the presented methods, we compare the results of our methods with those from real-world throwing experiments that were previously conducted on DLR David [9]. Finally, our approach is applied to robot safety assessment, where the safety characteristics of both the elastic and a hypothetically rigid version of DLR David are compared in terms of the Safety Map framework [12].

II. Considered Dynamics

The considered elastic joint robot dynamics are [13]

$$\boldsymbol{M}(\boldsymbol{q})\ddot{\boldsymbol{q}} + \boldsymbol{C}(\boldsymbol{q},\dot{\boldsymbol{q}})\dot{\boldsymbol{q}} + \boldsymbol{g}(\boldsymbol{q}) = \boldsymbol{\tau}_J(\boldsymbol{\theta},\boldsymbol{q})\,, \tag{1a}$$

$$\boldsymbol{B}\ddot{\boldsymbol{\theta}} + \boldsymbol{\tau}_J(\boldsymbol{\theta},\boldsymbol{q}) = \boldsymbol{\tau}_m\,, \tag{1b}$$

with $\boldsymbol{\theta} \in \mathbb{R}^n$ and $\boldsymbol{q} \in \mathbb{R}^n$ representing the motor and link positions. The motor and link inertia matrices are denoted by $\boldsymbol{B} \in \mathbb{R}^{n\times n}$ and $\boldsymbol{M}(\boldsymbol{q}) \in \mathbb{R}^{n\times n}$, the Coriolis matrix by $\boldsymbol{C}(\boldsymbol{q},\dot{\boldsymbol{q}}) \in \mathbb{R}^{n\times n}$, and the gravity vector by $\boldsymbol{g}(\boldsymbol{q}) \in \mathbb{R}^n$. The motor torque is denoted by $\boldsymbol{\tau}_m \in \mathbb{R}^n$ and possibly non-linear elastic joint torque by $\boldsymbol{\tau}_J(\boldsymbol{\theta},\boldsymbol{q}) \in \mathbb{R}^n$, which depends on the elastic deflection $\boldsymbol{\varphi} = \boldsymbol{\theta} - \boldsymbol{q}$. In the rigid joint case, the links are directly driven by the motor torques, i.e., (1a) constitutes the dynamics where $\boldsymbol{\tau}_J(\boldsymbol{\theta},\boldsymbol{q})$ is replaced by $\boldsymbol{\tau}_m$. As we are interested in the maximum performance in terms of speed, we do not consider link-side damping, which generally decreases the velocity.[1] The Jacobian matrix $\boldsymbol{J}(\boldsymbol{q}) \in \mathbb{R}^{m\times n}$ associated to the end-effector can be decomposed as $\boldsymbol{J}(\boldsymbol{q}) = [\boldsymbol{J}_\nu(\boldsymbol{q})^\mathsf{T}, \boldsymbol{J}_\omega(\boldsymbol{q})^\mathsf{T}]^\mathsf{T}$, where $\boldsymbol{J}_\nu(\boldsymbol{q})$ and $\boldsymbol{J}_\omega(\boldsymbol{q})$ relate joint velocities to translational and angular Cartesian velocities, respectively.

By assuming that the motor-side dynamics are typically much faster than the link-side dynamics and that the motors always provide enough torque to accelerate the motor shaft and compensate for the elastic joint torque, we may model the motors as velocity sources [9]. In the reduced model, the link-side dynamics (1a) remain the same, while the motor dynamics (1b) simply become $\boldsymbol{\theta} = \int \dot{\boldsymbol{\theta}}\, dt + \boldsymbol{\theta}_0$.

We consider the motor velocity constraint $|\dot{\boldsymbol{\theta}}| \le \dot{\boldsymbol{\theta}}_{\max}$ and the elastic deflection constraint $|\boldsymbol{\varphi}| \le \boldsymbol{\varphi}_{\max}$, which are the most important real-world constraints besides motor torque. We assume that the constraints are symmetric, which is the case for most systems. The maximum elastic deflection depends on the spring energy storage capacity and usually the selected stiffness setup, if stiffness can be adjusted. In the DLR FSJ joint [14], e. g., a stiff setup allows for a lower maximum deflection than a soft stiffness setup. In some VSA actuators, $\boldsymbol{\varphi}_{\max}$ is constant, irrespective of the selected stiffness. Typically, not the entire potential elastic energy can be utilized for energy storage and release. The available energy can be limited by a) spring pretension (e.g., in antagonistic setups), b) the stiffness setup, and c) the maximum possible elastic deflection (see above). In the following, we denote the overall amount of spring energy that can be actively exploited, e. g., to perform explosive motions, by $U_{S,\mathrm{dyn}} = \sum_{i=1}^{n} U_{S,\mathrm{dyn},i}$, where $U_{S,\mathrm{dyn},i}$ denotes the elastic energy in joint i. For VSA joints, we assume $U_{S,\mathrm{dyn},i}$ to be the largest possible energy.

[1]The methods in this work could be extended to visco-elastic joints with the results reported in [6], [7], for example.

III. Maximum Cartesian Endpoint Velocity

In the following, we summarize the related work on the maximum achievable velocities of rigid and elastic joint robots. Then, the problem definition and our approach are described in detail. Afterwards, we propose hypotheses for determining the maximum Cartesian endpoint velocity of elastic joint robots and exemplify the theory using a planar 3R robot.

A. Related Work

1) Rigid Joint Robots: The manipulability ellipsoid and polytope are well-established tools for analyzing the Cartesian velocity capabilities of rigid joint robots for a given configuration [2]. From a computational point of view, ellipsoids are more tractable than polytopes. However, we only consider polytopes in this letter, as they represent all achievable velocities while the ellipsoids only constitute a subset of these. Consider the motor velocity constraint $|\dot{\boldsymbol{q}}| \le \dot{\boldsymbol{q}}_{\max}$, where $\dot{\boldsymbol{q}}_{\max}$ is the maximum motor velocity. For the sake of simplicity, we again assume that the motor velocity bounds are symmetric. The $2n$ motor velocity bounds form a hyperrectangle in joint space which has 2^n vertices. The translational manipulability polytope in the so-called *weak sense*, denoted by $\mathrm{TMP}_{\mathrm{ws}}$, is obtained by transforming the joint-space hyperrectangle to Cartesian space via $\boldsymbol{\nu} = \boldsymbol{J}_\nu(\boldsymbol{q})\dot{\boldsymbol{q}}$, where $\boldsymbol{\nu} \in \mathbb{R}^3$ denotes the translational velocity. Weak sense means that the angular velocity $\boldsymbol{\omega} = \boldsymbol{J}_\omega(\boldsymbol{q})\dot{\boldsymbol{q}}$ may be non-zero. In case of redundancy ($m < n$) the hyperrectangle is mapped to a space of lower dimension. As a result, the boundary of the Cartesian polytope is defined by less than 2^n vertices because there are internal vertices. For a 3R planar robot[2] that performs a translational task ($n = 3, m = 2$), we obtain $2^3 = 8$ vertices in joint space and typically six vertices in Cartesian space which form the polytope; see Fig. 1. To obtain the TMP in the so-called *strong sense* (i.e., purely translational motions), denoted by $\mathrm{TMP}_{\mathrm{ss}}$, in case of redundancy, we require the motor speeds that are part of the null space of $\boldsymbol{J}_\omega(\boldsymbol{q})$ and fulfill the velocity constraints at the same time, i. e., $\{\dot{\boldsymbol{q}} \,|\, \dot{\boldsymbol{q}} \in \mathcal{N}(\boldsymbol{J}_\omega(\boldsymbol{q})) \,\&\, |\dot{\boldsymbol{q}}| \le \dot{\boldsymbol{q}}_{\max}\}$. An algorithm to determine such motor velocities is provided in [15], which was originally proposed for force polytope analysis. The maximum possible velocity (either weak or strong sense) in a certain Cartesian unit direction $\boldsymbol{u} \in \mathbb{R}^3$ can be determined with the line clipping algorithm proposed in [16], for example. Please note that the strong sense TMP is a subset of the weak sense TMP.

[2]The length of each robot link is 0.5 m, a 2 kg point mass is located at the distal end of each link. The maximum symmetric velocity of each motor is 2 rad/s and the joint configuration is $\boldsymbol{q} = [110, -70, -70]^\mathsf{T}\,^\circ$.

2) Elastic Joint Robots: a) 1-DOF: In robotics literature, many authors investigated the optimality principles for visco-elastic and variable impedance joints [3]–[7], [17]. If no damping is present and the elastic energy is limited, then the maximum achievable link velocity of a planar, linear 1-DOF elastic joint with mass m can be expressed as the sum of the maximum motor velocity and a term $\Delta\dot{q}$ coming from spring energy and release[3]

$$\dot{q}_{\max} = \dot{\theta}_{\max} + \Delta\dot{q} = \dot{\theta}_{\max} + \sqrt{\frac{2U_{S,\mathrm{dyn}}}{m}}\,. \tag{2}$$

It is reached when all the potential spring energy has been converted to link kinetic energy ($\frac{1}{2}m\Delta\dot{q}^2 = U_{S,\mathrm{dyn}}$) while the link is traveling in the motor inertial frame of reference. The time-optimal trajectory to reach this velocity is provided in [4], results for visco-elastic joints can be found in [6], [7]. Instead of formulating the maximum link velocity as the sum of a motor and a spring term, it is also possible to express the benefit of the elastic mechanism on link velocity in terms of a so-called speed gain $\epsilon = \dot{q}_{\max}/\dot{\theta}_{\max} \geq 1$ [4]. When the system has reached the maximum link velocity, then the total system energy is

$$V_f = \frac{1}{2}m\dot{q}_{\max}^2\,, \tag{3a}$$

$$= \underbrace{\frac{1}{2}m\dot{\theta}_{\max}^2 + U_{S,\mathrm{dyn}}}_{V_{ch}} + \dot{\theta}_{\max}\sqrt{2mU_{S,\mathrm{dyn}}}\,. \tag{3b}$$

It is given by the sum of V_{ch}, the energy that the system has when the link travels with maximum motor speed and the spring is fully charged, and a term required to keep the maximum motor velocity while compensating for the elastic joint torque.

b) 2 to n-DOF: In [9]–[11], it was investigated how the elastic energy of systems with two or more DOF can be exploited to realize explosive motions, in particular the throwing of a ball as far as possible. The influence of coupling stiffness, nonlinear dynamics, and nonlinear elasticity with stiffness adjustment on unimodal and sequential-type motions was analyzed. Optimal trajectories were found both for academic and real-world systems like DLR David and a MACCEPA robot. Based on the simulation and experimental results, basic power flow and energy transfer mechanisms like consecutive loading and unloading of the springs for sequential type motions were investigated. Furthermore, comparisons were made to human studies on explosive motions.

B. Problem Definition & Approach

Up to now, explosive motions together with the maximum peak velocity were mainly derived via optimal control. Usually, such (numerical) techniques are computationally very costly, time consuming, and require accurate modeling of the complex system dynamics. Especially in the early design phase of the robot mechanics where quick iterations are desirable, but also in task and motion planning it is essential that the maximum achievable TCP velocities for a certain robot configuration can be estimated in minimum time. For such applications, optimal control methods are hardly suitable due to their large computational effort.

[3]Please note that not every achievable link velocity can be expressed in this convenient form.

In this work, we seek a representation of the maximum possible Cartesian endpoint velocities for elastic joint robots that a) is simple and computationally inexpensive to derive and b) estimates the achievable velocities with sufficient accuracy. Although important for real-world implementation and for understanding the energy transfer mechanisms, the derivation of the associated (time-optimal) trajectories is not considered in this letter. Inspired by the velocity polytope for rigid joint robots, we want to determine the representation of the maximum Cartesian velocities for a certain joint configuration. We assume that the elastic energy can be locally transferred to kinetic energy around the desired link configuration $\boldsymbol{q}_d$ via internal spring deflection and release. In this letter, we consider gravity-free elastic joint robots. We focus on the energy storage and release mechanism of the spring, the influence of gravitational potential energy on the maximum achievable velocity should be investigated in future work. We are interested in determining those velocities that can be reached from equilibrium by injecting energy via control and without external contact being applied.

We propose the two main hypotheses H1 and H2 to derive the achievable TCP velocities. Hypothesis H1 is inspired by (3) and relies on the assumption that a certain amount of energy can be injected into the system which can be converted to link kinetic energy. H1 has two sub-hypotheses $\mathrm{H1}_a$ and $\mathrm{H1}_b$. Hypothesis H2 is inspired by (2) and extends the TMP approach from the rigid to the elastic joint case. The three sub-hypotheses of H2 are denoted by $\mathrm{H2}_a$, $\mathrm{H2}_b$, and $\mathrm{H2}_c$. Starting with H1, we describe all the hypotheses in the following. The theory is applied to the 3R planar robot that was introduced previously. Every joint of this robot is now equipped with a linear spring that can store up to 2 J potential energy. An overview of the results for all hypotheses is provided in Fig. 3.

C. Hypothesis H1

In our first hypothesis H1, we assume that we can inject a certain amount of energy V into the system that can be converted (solely) to link kinetic energy. By extending (3) from 1-DOF to n-DOF we obtain the candidate energies

$$\mathbf{H1}_a \quad V_{ch} = \frac{1}{2}\dot{\boldsymbol{\theta}}_{\max}^{\mathsf{T}}\boldsymbol{M}(\boldsymbol{q})\dot{\boldsymbol{\theta}}_{\max} + U_{S,\mathrm{dyn}}\,, \tag{4a}$$

$$\mathbf{H1}_b \quad V_f = V_{ch} + \dot{\boldsymbol{\theta}}_{\max}^{\mathsf{T}}\sqrt{2\boldsymbol{M}(\boldsymbol{q})}\sqrt{\boldsymbol{u}_{S,\mathrm{dyn}}}\,, \tag{4b}$$

where $\boldsymbol{u}_{S,\mathrm{dyn}} = [U_{S,\mathrm{dyn},i}, \ldots, U_{S,\mathrm{dyn},n}]^{\mathsf{T}}$. For V_{ch}, the links have the same velocities as the motors and all springs are fully deflected. The energy V_f is the sum of V_{ch} and an additional term analogous to (3). In sub-hypothesis $\mathrm{H1}_a$ we assign $V = V_{ch}$ and in $\mathrm{H1}_b$ $V = V_f$. By equating the total energy with the link kinetic energy $\frac{1}{2}\dot{\boldsymbol{q}}^{\mathsf{T}}\boldsymbol{M}(\boldsymbol{q})\dot{\boldsymbol{q}} = V$ and rearranging the terms we get

$$\dot{\boldsymbol{q}}^{\mathsf{T}}\frac{\boldsymbol{M}(\boldsymbol{q})}{2V}\dot{\boldsymbol{q}} = 1\,, \tag{5}$$

which describes an ellipsoid in joint space. Equation (5) represents all joint velocities which are feasible given the energy V. Using the translational Jacobian matrix $\boldsymbol{J}_\nu(\boldsymbol{q})$ we can now transform the velocities (5) to Cartesian space. We obtain the same result when inserting $\dot{\boldsymbol{q}} = \boldsymbol{J}_\nu(\boldsymbol{q})^+\boldsymbol{\nu}$, where $\boldsymbol{J}_\nu(\boldsymbol{q})^+$ is the generalized inverse of $\boldsymbol{J}_\nu(\boldsymbol{q})$, into the previous equation, which

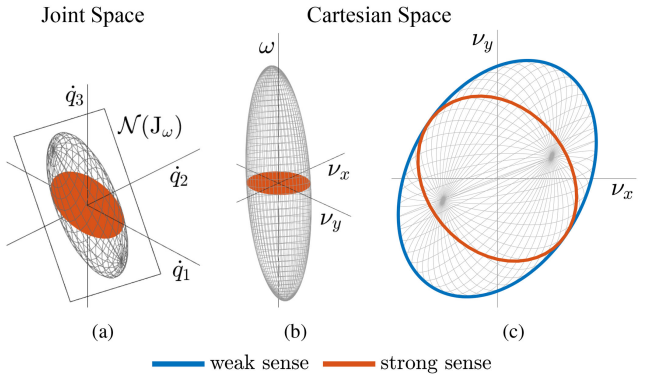

Fig. 2. Hypothesis H1: Strong and weak sense velocities in joint space (a) and Cartesian space (b), (c).

yields

$$\boldsymbol{\nu}^{\mathsf{T}} \frac{(\boldsymbol{J}_\nu(\boldsymbol{q})\boldsymbol{M}(\boldsymbol{q})^{-1}\boldsymbol{J}_\nu(\boldsymbol{q})^{\mathsf{T}})^{-1}}{2V}\boldsymbol{\nu} \leq 1\,. \tag{6}$$

This ellipsoid is the weak sense representation of the achievable translational velocities. The result for the 3R robot is illustrated in Fig. 2 and Fig. 3(a), (b). In order to determine the strong sense velocities, one needs to find the intersection of the nullspace $\mathcal{N}(\boldsymbol{J}_\omega(\boldsymbol{q}))$ and the ellipsoid (5), i.e., the velocities that satisfy $\{\dot{\boldsymbol{q}} \,|\, \dot{\boldsymbol{q}} \in \mathcal{N}(\boldsymbol{J}_\omega(\boldsymbol{q})) \,\&\, \frac{1}{2}\dot{\boldsymbol{q}}^{\mathsf{T}}\boldsymbol{M}(\boldsymbol{q})\dot{\boldsymbol{q}} = V\}$. The shape of the intersection depends on the dimension of $\mathcal{N}(\boldsymbol{J}_\omega(\boldsymbol{q}))$. For example, if $n - m_{J_\omega} = 1$, where m_{J_ω} is the number of rows of $\boldsymbol{J}_\omega(\boldsymbol{q})$, then the null space is represented by a line in $\mathbb{R}^n$, for $m_{J_\omega} = 1, n \geq 2$ it is a hyperplane with dimension $n-1$. For our 3R robot, the nullspace of $\boldsymbol{J}_\omega(\boldsymbol{q})$ is represented by a two-dimensional plane in $\mathbb{R}^3$; see Fig. 2(a). Practically, one can obtain the boundary of the intersection as follows:

1) Determine the joint velocities $\dot{\boldsymbol{q}}$ that are located on the unit sphere $\dot{\boldsymbol{q}}^{\mathsf{T}}\dot{\boldsymbol{q}} = 1$.
2) Project these velocities onto the null space of $\boldsymbol{J}_\omega(\boldsymbol{q})$ with $\dot{\boldsymbol{q}}_{\mathcal{N}_\omega} = (\boldsymbol{I} - \boldsymbol{J}_\omega(\boldsymbol{q})^{+}\boldsymbol{J}_\omega(\boldsymbol{q}))\dot{\boldsymbol{q}}$. The velocities are still located within the unit sphere.
3) Scale the null space velocities onto the boundary of the ellipsoid (5) via

$$\dot{\boldsymbol{q}}_{e,\mathcal{N}_\omega} = \sqrt{\frac{2V}{\dot{\boldsymbol{q}}_{\mathcal{N}_\omega}^{\mathsf{T}}\boldsymbol{M}(\boldsymbol{q})\dot{\boldsymbol{q}}_{\mathcal{N}_\omega}}}\dot{\boldsymbol{q}}_{\mathcal{N}_\omega}\,. \tag{7}$$

The Cartesian velocities in the strong sense are finally given by $\boldsymbol{\nu} = \boldsymbol{J}_\nu(\boldsymbol{q})\dot{\boldsymbol{q}}_{e,\mathcal{N}_\omega}$. The result for the 3R robot is illustrated in Fig. 2(c). The comparison of the weak and strong sense velocities for both the rigid (motors only) and the elastic joint 3R robot is shown in Fig. 3(a) ($\mathrm{H1}_a$) and (b) ($\mathrm{H1}_b$). It can be observed that the maximum achievable endpoint velocity of the elastic robot is much larger than the velocity of the rigid counterpart. Because the energy V_f is larger than V_{ch} (cf. (4)), hypothesis $\mathrm{H1}_b$ provides larger velocities than hypothesis $\mathrm{H1}_a$.

D. Hypothesis H2

In hypothesis H1, the Cartesian velocity ellipsoid was obtained via a scalar kinetic energy that comprised the contribution of both the motors and the springs. As far as the motors are concerned (in other words, the rigid version of the robot) one can directly determine the feasible Cartesian velocity polytope according to Sec. III-A without the need of conversion to an (intermediate) energy. In our second hypothesis H2, we want to start from this motor velocity polytope and add the velocities that come from the release of stored spring energy. As in the 1-DOF case described previously (see (2)), we assume that the maximum possible link velocity can be written in the form

$$\dot{\boldsymbol{q}}_{\max} = \dot{\boldsymbol{\theta}}_{\max} + \Delta\dot{\boldsymbol{q}}\,, \tag{8}$$

where $\Delta\dot{\boldsymbol{q}}$ represents the velocity gain attributed to the release of elastic energy. We assume that the entire elastic energy can be converted to link kinetic energy. To determine $\Delta\dot{\boldsymbol{q}}$, we formulate three sub-hypotheses $\mathrm{H2}_a$–$\mathrm{H2}_c$ on the energy conversion mechanism.

- **H2**$_a$ Each joint has a maximum link velocity which consists of the maximum motor velocity plus a term provided by the spring in the respective joint only. It is assumed that there is no inertial coupling between the links, i. e., n independent mass-spring systems are considered.
- **H2**$_b$ Like $\mathrm{H2}_a$ with the difference that the inertia about each joint is given by the configuration-dependent inertia of all successive links, which are assumed to be rigidly coupled.
- **H2**$_c$ The available spring potential energy is converted to link kinetic energy while making no assumptions on how a particular spring contributes to the maximum possible link velocity.

In the following, we explain each sub-hypothesis and apply the theory to the 3R robot. The resulting velocities are illustrated in Fig. 3(c)–(e).

a) Hypothesis $\mathrm{H2}_a$. In the same spirit as the related work on 1-DOF, $\mathrm{H2}_a$ assumes that each elastic joint has a certain maximum link velocity. The motivation behind this is to extend the TMP from the rigid joint to the elastic joint case in a very straightforward manner. Let us assume that there is no dynamic coupling between the links, in other words, we have n independent mass-spring systems, and that the entire elastic energy can be converted to link kinetic energy. In each joint we have a motor with the maximum velocity $\dot{\theta}_{\max,i}$, a spring with available energy $U_{S,\mathrm{dyn},i}$, and the link inertia ${}^{i}m_i$ about the current axis. We can again use (2) to determine the maximum link velocity

$$\dot{q}_{\max,i} = \dot{\theta}_{\max,i} + \sqrt{\frac{2U_{S,\mathrm{dyn},i}}{{}^{i}m_i}}, \quad i = 1,\ldots,n\,, \tag{9}$$

in each joint. We can now derive the weak sense velocity polytope by transforming the joint space hyperrectangle $|\dot{\boldsymbol{q}}| \leq \dot{\boldsymbol{q}}_{\max}$ to Cartesian space via $\boldsymbol{J}_\nu(\boldsymbol{q})$. This is the same procedure as for rigid joint robots, where $\dot{\boldsymbol{q}}$ is the motor velocity. The derivation of the strong sense velocity polytope also remains the same, cf. Sec. III-A1. The TMPs for the rigid and elastic case are illustrated in Fig. 3(c)), which have the same shape, but are different in size, meaning the elastic joint robot can reach higher velocities.

b) Hypothesis $\mathrm{H2}_b$. Previously, we assumed that the inertia about joint i is given by the decoupled link inertia ${}^{i}m_i$. A more conservative approach is to assume that all link inertias from joint i to n are rigidly coupled. The maximum joint velocity in this case is again determined with (9), where ${}^{i}m_i$ is now being replaced by $M_{i,i}$, the i-th element of the main diagonal of $\boldsymbol{M}(\boldsymbol{q})$. The results for the 3R robot are illustrated in Fig. 3(d).

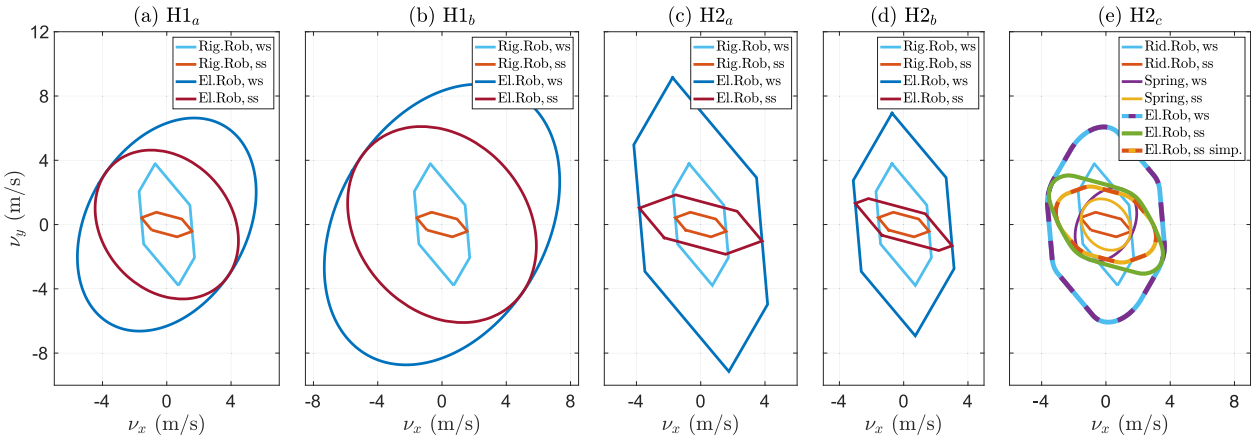

Fig. 3. Maximum Cartesian endpoint velocity for the 3R robot (configuration depicted in Fig. 1): Motor velocity polytopes (Rig.Rob) and the velocities of the elastic joint robot obtained by the hypotheses (El.Rob). Subscripts: ws: weak sense, ss: strong sense.

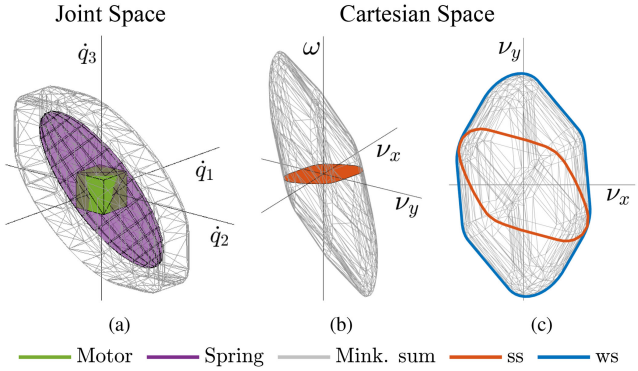

Fig. 4. Hypothesis H2$_c$: (a) Motor velocity bounds, spring ellipsoid (10), and Minkowski sum, (b) transformation of joint-space Minkowski sum to Cartesian space together with the strong sense velocities ($\boldsymbol{\omega} = \mathbf{0}$), (c) weak and strong sense velocities.

Compared to the previous hypothesis H2$_a$, H2$_b$ provides lower velocities because the inertia about the joints is larger.

c) Hypothesis H2$_c$. In hypotheses H2$_a$ and H2$_b$, it was assumed that the potential energy of every spring is converted to kinetic energy in the particular joint. This allowed us to apply the TMP theory from rigid joint manipulators to elastic joint robots. In hypothesis H2$_c$ we do not assume that each joint has a certain maximum velocity, but rather that the overall available elastic energy is converted to kinetic link energy. Similar to hypothesis H1 (cf. (5)), the joint space ellipsoid

$$\Delta\dot{\boldsymbol{q}}^{\mathsf{T}} \frac{\boldsymbol{M}(\boldsymbol{q})}{2U_{S,\mathrm{dyn}}} \Delta\dot{\boldsymbol{q}} = 1\,, \tag{10}$$

represents the contribution of the spring to the achievable link velocity. According to (8), we now determine the geometric sum, i. e., the Minkowski sum[4] of the motor and spring velocities. The result for the 3R robot is illustrated in Fig. 4. The joint velocities obtained by the Minkowski sum can be transformed to Cartesian space via $\boldsymbol{J}_\nu(\boldsymbol{q})$, which gives us the weak sense representation; see Fig. 4(c). To derive the strong sense velocities, one needs to find the intersection of the joint-space Minkoswki sum and the nullspace of $\boldsymbol{J}_\omega(\boldsymbol{q})$, or the Cartesian velocities that satisfy $\boldsymbol{\omega} = \mathbf{0}$. For the 3R robot, we applied the 3D clipping algorithm [16] to find the intersection of the Cartesian Minkowski sum with the ν_x/ν_y-plane; see Fig. 4(b), (c). For systems/tasks with more DOF, it can become difficult to derive the H2$_c$ strong sense velocities. However, a subset of the feasible velocities can be determined rather easily by first computing the strong sense representation of the motor and spring velocities independently (see Sec. III-A1 and (7)) and then calculating the Minkowski sum of both representations. The sum of the two nullspace velocities also belongs to the nullspace $\mathcal{N}(\boldsymbol{J}_\omega(\boldsymbol{q}))$. The result for this simplified approach is illustrated in Fig. 3(e) for the 3R robot. In the figure, the motor polytope (red) is added to the spring ellipse (yellow), which results in the red/yellow dashed representation. It can be observed that these velocities are a subset of the achievable strong sense velocities, which are represented by a green line.

[4]The Minkowski sum for two sets C_1 and C_2 is defined as $C_1 \oplus C_2 = \{c_1 + c_2 | c_1 \in C_1, c_2 \in C_2\}$, i. e., the resulting set contains the sum of every element from C_1 and every element from C_2.

IV. Verification via Optimal Control

In order to verify our hypotheses, we formulate an optimal control problem that can be solved to find the maximum feasible endpoint velocities and the according robot trajectories. The problem is numerically solved for the elastic 3R robot, where we compare the optimal control solution to the velocities obtained by the hypotheses. Afterwards, this comparison is also done for the real-world throwing experiments previously conducted on the DLR David system [9], [18].

A. Problem Formulation

The motor position, link position, and velocity form the system state $\boldsymbol{x}_{\mathrm{opt}} = [\boldsymbol{x}_{\mathrm{opt},1}^{\mathsf{T}}, \boldsymbol{x}_{\mathrm{opt},2}^{\mathsf{T}}, \boldsymbol{x}_{\mathrm{opt},3}^{\mathsf{T}}]^{\mathsf{T}} = [\boldsymbol{\theta}^{\mathsf{T}}, \boldsymbol{q}^{\mathsf{T}}, \dot{\boldsymbol{q}}^{\mathsf{T}}]^{\mathsf{T}}$, the control input is the motor velocity $\boldsymbol{w} = \dot{\boldsymbol{\theta}}$, which is bounded by $|\boldsymbol{w}| \leq \dot{\boldsymbol{\theta}}_{\max}$. The cost function for the optimal control problem has the standard form

$$J_{\mathrm{opt}} = \phi(t_f, \boldsymbol{x}_{\mathrm{opt}(t_f)}) + \int_{t_0}^{t_f} L(t, \boldsymbol{x}_{\mathrm{opt}}, \boldsymbol{w})\, dt\,, \tag{11}$$

where $\phi(t_f, \boldsymbol{x}_{\mathrm{opt}(t_f)})$ is the Mayer term and $L(t, \boldsymbol{x}_{\mathrm{opt}}, \boldsymbol{w})$ the Lagrange term. The initial and final time are denoted by t_0 and t_f. We want to maximize the translational endpoint velocity in the desired Cartesian direction $\boldsymbol{u}_d$ and therefore select the Mayer term $\phi(t_f, \boldsymbol{x}_{\mathrm{opt}(t_f)}) = -\boldsymbol{u}_d^{\mathsf{T}} \boldsymbol{J}_\nu(\boldsymbol{x}_{\mathrm{opt},2}) \boldsymbol{x}_{\mathrm{opt},3}(t_f) +$

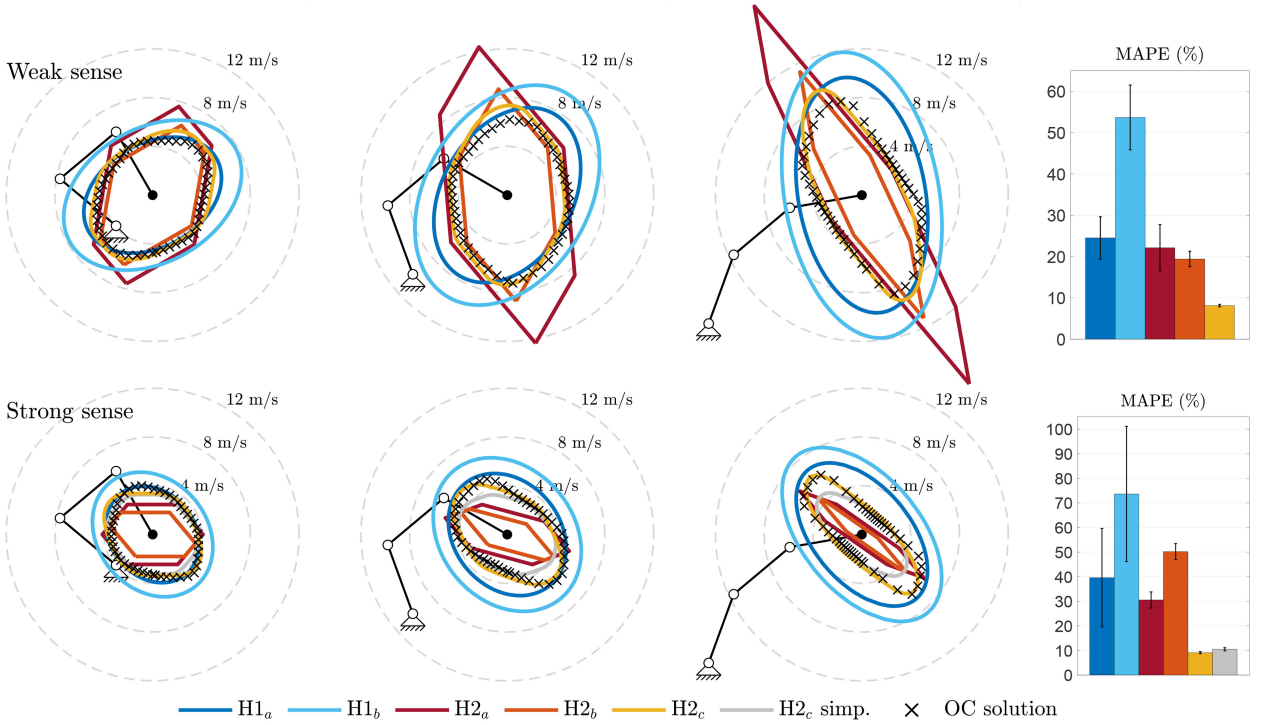

Fig. 5. 3R planar elastic joint robot: Comparison of the proposed methods and the optimal control solution which serves for verification. The weak sense results for three different goal configurations are depicted in the upper row, the strong sense results in the lower row. The bar graph on the right illustrates the mean average percentage error (MAPE) incl. variance w.r.t. the optimal control (OC) solution for each hypothesis. The smaller the error, the better the estimation of the maximum reachable TCP velocity.

ϵt_f. As the robot should reach the maximum velocity as fast as possible, our secondary goal is to minimize the final time. The Mayer term thus includes t_f, which is multiplied by a small positive constant ϵ. Theoretically, we do not need to specify a Lagrange term, however, from a practical point of view we select a small regularization term $L(t, \boldsymbol{x}_{\mathrm{opt}}, \boldsymbol{w}) = \frac{1}{2}\,\boldsymbol{w}^{\mathsf{T}}\boldsymbol{R}\boldsymbol{w}$ in order to smoothen the control input. Here, $\boldsymbol{R} \in \mathbb{R}^{n\times n}$ is a diagonal regularization matrix where the entries take rather low values. The optimal control problem is subject to the reduced elastic joint dynamics. The maximum spring deflection yields the path constraint $|\boldsymbol{x}_{\mathrm{opt},1} - \boldsymbol{x}_{\mathrm{opt},2}| \leq \boldsymbol{\varphi}_{\max}$. At $t = t_f$, the robot has the desired configuration $\boldsymbol{q}_d$ and the Cartesian velocity points in the desired direction $\boldsymbol{u}_d$, which yields the terminal constraints $\boldsymbol{x}_{\mathrm{opt},2}(t_f) = \boldsymbol{q}_d$ and $\frac{\boldsymbol{J}_\nu\,\boldsymbol{x}_{\mathrm{opt},3}(t_f)}{||\boldsymbol{J}_\nu\,\boldsymbol{x}_{\mathrm{opt},3}(t_f)||} = \boldsymbol{u}_d$. For the strong sense analysis, we add the terminal constraint $\boldsymbol{J}_\omega \boldsymbol{x}_{\mathrm{opt},3}(t_f) = \boldsymbol{0}$. In order to keep the motion as small as possible, we select the initial link position to be the same as the desired position, i. e., $\boldsymbol{x}_{\mathrm{opt},2}(t_0) = \boldsymbol{x}_{\mathrm{opt},2}(t_f) = \boldsymbol{q}_d$.

B. Results for the 3R Elastic Joint Robot

For the 3R robot, we select three goal configurations, namely $\boldsymbol{q}_{d,1} = [140, -100, -100]^{\mathsf{T}}\,^\circ$, $\boldsymbol{q}_{d,2} = [110, -70, -70]^{\mathsf{T}}\,^\circ$, and $\boldsymbol{q}_{d,3} = [70, 30, 30]^{\mathsf{T}}\,^\circ$, which reach from a folded to an outstretched configuration; see Fig. 5. The spring stiffness in each joint is 500 Nm/rad, the elastic energy was increased to 4.87 J ($\varphi_{\max} = 8\,^\circ$) in each joint, all other parameters remain the same. For each configuration, we solve the optimal control problem for 100 evenly-spaced Cartesian directions, i.e., points on the unit circle $\mathcal{S}^1$. The optimal trajectories were calculated with the numerical toolbox GPOPS[5] [19]. The robot trajectories obtained via optimal control (weak sense) are visualized in the attached video.

The results for the weak sense analysis are depicted in the upper row in Fig. 5, the results for the strong sense analysis in the lower row. The mean average percentage error (MAPE) (cumulative for all three configurations) incl. variance for each hypothesis w.r.t. the optimal control solution is illustrated in the bar graph on the right. For the considered robot, the best agreement with the optimal control results is accomplished with hypothesis H2$_c$, where the mean error (with negligible variance) is 8 % for weak sense velocities and 9 % for strong sense velocities. The MAPE for the other hypotheses is at least two times higher. H1$_b$ is the only hypothesis that provides a (over-)conservative approximation. Apparently, the robot's inertial coupling in $\boldsymbol{M}(\boldsymbol{q})$ has an influence on the achievable TCP velocities. The higher the inertial coupling the worse the estimation accuracy of hypotheses H2$_a$ and H2$_b$, where it is assumed that the links are decoupled. Hypotheses H1$_a$ and H1$_b$ consider inertial coupling, however, the contribution of both the motors and the springs is condensed in a scalar energy V that defines the size of the ellipsoids. The best solution for this robot is obtained by H2$_c$, where the TMP approach is extended from the rigid to the elastic joint case by summing the contributions of the motors and the springs and taking inertial coupling into account.

In terms of computation time, it took seven hours on average on an Intel(R) Core(TM) i7-8565U CPU @ 2.0 GHz with 16 GB

[5]Following parameters were used: $\boldsymbol{R} = \mathrm{diag}\{0.1, 0.1, 0.1\}$, $\varepsilon = 0.001$, mesh tolerance: 0.001, no. mesh iterations: 3, no. nodes per interval: min: 6, max: 12.

TABLE I
3R PLANAR ELASTIC JOINT ROBOT: TIME REQUIRED TO COMPUTE THE MAXIMUM TCP VELOCITIES ILLUSTRATED IN FIG. 5

Rigid joint	Elastic joint					
	OC	$H1_a$	$H1_b$	$H2_a$	$H2_b$	$H2_c$
45 ms	$\approx$ 2 days	53 ms	53 ms	46 ms	46 ms	860 ms

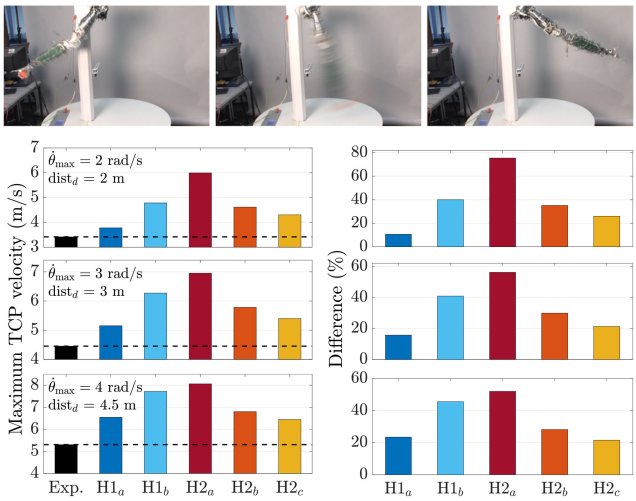

(a) 2-DOF throwing experiments for different maximum motor velocities $\dot{\theta}_{\max}$ and desired throwing distances dist_d.

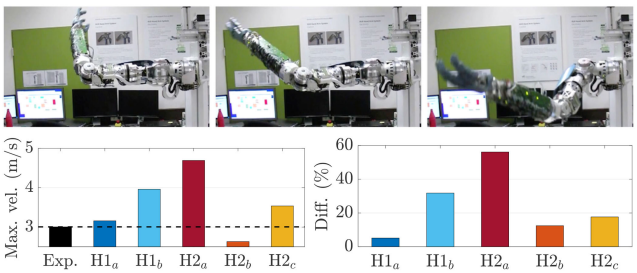

(b) 3-DOF throwing experiment with $\dot{\theta}_{\max} = 2\,\text{rad/s}$.

Fig. 6. Previous throwing experiments on the DLR David system [9], [18]: Maximum measured TCP velocity and difference (absolute and relative) w.r.t. the velocities estimated by the proposed hypotheses.

RAM (MATLAB 2020a) to compute the (100) optimal control solutions for each configuration and weak/strong sense representation in Fig. 5, i.e., approx. a full two days for all results. In contrast, only 1.1 s were required in total to compute the velocities resulting from all the hypotheses shown in Fig. 5. An overview of the cumulated computation times for the 3R is provided in Tab. I. The time required to compute $H1_a$–$H2_b$ is similar to the rigid joint case. $H2_c$ requires more time because the derivation of the strong sense representation is computationally costly.

C. Evaluation of Previous DLR David Experiments

Next, we compare the results of our presented methods with those from the ball throwing experiments that were previously conducted on the DLR David system [9]; see Fig. 6 and the video in [18]. The goal of the optimal control problem in [9] was to throw a ball to a certain target distance for a fixed final time. In the 2-DOF (planar) experiments (see Fig. 6(a)), joints 1 and 4 were actuated. The excitation trajectories were generated for different motor velocity limits and target distances. In Fig. 6(a), we show the results for $\dot{\theta}_{\max} = 2, 3$, and 4 rad/s. For each considered motor velocity limit, we select the experiment with the farthest achieved throwing distance. The maximum measured TCP velocities are illustrated in Fig. 6(a). In the figure, these velocities are compared to the TCP velocities (absolute and relative) estimated by the proposed hypotheses. In the 3-DOF (three-dimensional space) experiment, joints 2–4 (shoulder and elbow) were actuated, the maximum motor velocity was limited to 2 rad/s. The results are depicted in Fig. 6(b).

Please note that the problem formulation of the previous experiments is a bit different from the one in this letter. In [9] the goal was to achieve a desired throwing distance and not the maximum possible throwing distance, respectively TCP velocity. This is reflected in the both the desired optimal control and the actual robot trajectories, where the maximum motor velocity and elastic deflection are typically not fully exploited. In contrast, in the 3R optimal control solution, both quantities reach their limits at a certain position along the trajectory. It is therefore to be expected that the velocities obtained by our hypotheses are larger than the velocities observed in the experiments. Nevertheless, hypotheses $H1_a$ and $H2_c$ agree reasonably well with the experimental results. Regarding the 2-DOF experiments, we obtain 11% (2 rad/s), 16% (3 rad/s), and 23% (4 rad/s) difference w.r.t. the experiment for $H1_a$, for $H2_c$ the difference is 26% (2 rad/s), 21% (3 rad/s), and 21% (4 rad/s). Concerning the 3-DOF experiment, the difference is 5% for $H1_a$ and 18% for $H1_c$. In our comparison for the 2-DOF experimental series, the difference between estimated and measured TCP velocity increases with maximum motor velocity; see Fig. 6(a). In [9], the tracking error in motor position deteriorated for desired motor velocities $\geq$4 rad/s, which resulted in (slightly) lower endpoint velocities than expected. The authors of [9] explained this with unmodeled dynamics and friction. Furthermore, the assumption that the motors can be regarded as velocity sources has limitations for high motor accelerations.

V. APPLICATION: SAFETY MAP FOR DLR DAVID

Besides analyzing peak performance, one of our major motivations for determining the maximum Cartesian endpoint velocity of elastic joint robots is to derive the safety characteristics of this robot type. We want to represent elastic joint robots in the Safety Map framework [12], which allows us to compare different robots (i.e., also rigid joint manipulators or mobile robots) to human injury data. In this section, we apply our theory to derive the Safety Map representation of the DLR David system [20]. We want to determine the reflected robot mass [21] and maximum velocity (weak sense) in the direction of the three principal Cartesian directions X, Y, and Z for the red workspace area depicted in Fig. 7 (left)[6]. The Safety Map representation is determined for both the elastic and a hypothetically rigid version of the robot. The links on the rigid version of David are driven by the motors only and $\boldsymbol{M}(\boldsymbol{q})$ includes both the motor and

[6]We only consider actuation of the first four robot joints and ignore motions of the wrist and hand. The maximum velocity of each motor is 8.51 rad/s, the maximum available elastic energy in each FSJ joint is 5.3 J [14]. The considered box has a 25 cm edge length, the center is located at $[-0.2035, -0.45, -0.2]^{\mathsf{T}}$ m w.r.t. the robot base located in the shoulder.

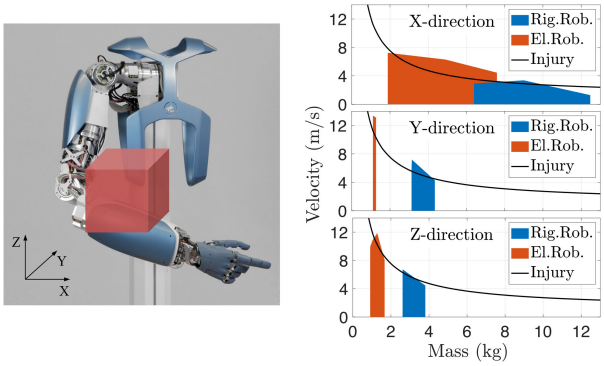

Fig. 7. Application of our approach to safety assessment of the DLR David system in the Safety Map framework [12]. The reflected mass and velocity ranges of the elastic (red) and hypothetically rigid David (blue) are compared to the chest injury threshold (black line) by means of the Compression Criterion (CC, threshold: 22 mm chest deflection). Every mass/velocity pair above the threshold corresponds to (at least) 5% probability of serious chest injury. This threshold was derived from Lobdell's well-known chest collision model [24].

the link inertia. To determine the maximum endpoint velocities for elastic David, we use hypothesis $H2_c$, because it provided good and, more importantly, conservative velocity estimates for David previously. The Safety Maps are illustrated in Fig. 7. It can be observed that elastic David has a lower mass range, but it can reach much higher velocities than the rigid counterpart. These results agree well with our expectation and previous results [3], [22], [23]. In Fig. 7 we also depict the threshold for the occurrence of blunt chest injury by means of the so-called Compression Criterion [24]. Both rigid and elastic David are capable of harming the human when high-speed motions are performed in this workspace area. When operating an elastic robot at velocities equal to its rigid counterpart, the elastic robot is the safer option. However, as the impact velocity typically has a stronger influence on injury probability than the reflected mass [25], it is possible that the elastic joint robot poses a larger threat to the human for certain body parts and collision scenarios than a rigid joint robot.

VI. Conclusion

In this work, we proposed and evaluated several approaches to determine the maximum achievable Cartesian endpoint velocities for gravity-free elastic joint robots. The peak TCP velocity is an important characteristic for robot design, motion and task planning to assess and optimize collision safety and performance. In contrast to numerical optimal control tools, which are typically employed in literature, our methods require minimal computational effort. We verified our methods for a simulated 3R robot. Also for the previous ball throwing experiments conducted on DLR David we observed a reasonable agreement between the real and the estimated velocities. Finally, we applied the theory to the global robot safety assessment and compared the safety performance of DLR David with a hypothetically rigid version of this robot and human injury data in terms of the Safety Map framework.

References

[1] B. Vanderborght *et al.*, "Variable impedance actuators: A review," *Robot. Auton. Syst.*, vol. 61, no. 12, pp. 1601–1614, 2013.
[2] T. Yoshikawa, "Manipulability of robotic mechanisms," *Int. J. Robot. Res.*, vol. 4, no. 2, pp. 3–9, 1985.
[3] S. Haddadin, T. Laue, U. Frese, S. Wolf, A. Albu-Schäffer, and G. Hirzinger, "Kick it with elasticity: Safety and performance in human-robot soccer," *Robot. Auton. Syst.*, vol. 57, no. 8, pp. 761–775, 2009.
[4] S. Haddadin, K. Krieger, N. Mansfeld, and A. Albu-Schäffer, "On impact decoupling properties of elastic robots and time optimal velocity maximization on joint level," in *Proc. IEEE/RSJ Int. Conf. Intell. Robots Syst.*, 2012, pp. 5089–5096.
[5] M. Garabini, A. Passaglia, F. Belo, P. Salaris, and A. Bicchi, "Optimality principles in stiffness control: The VSA kick," in *Proc. IEEE Int. Conf. Robot. Automat.*, 2012, pp. 3341–3346.
[6] M. C. Özparpucu and S. Haddadin, "Optimal control for maximizing link velocity of visco-elastic joints," in *Proc. IEEE/RSJ Int. Conf. Intell. Robots Syst.*, 2013, pp. 3035–3042.
[7] N. Mansfeld and S. Haddadin, "Reaching desired states time-optimally from equilibrium and vice versa for visco-elastic joint robots with limited elastic deflection," in *Proc. IEEE/RSJ Int. Conf. Intell. Robots Syst.*, 2014, pp. 3904–3911.
[8] M. Keppler and A. De Luca, "On time-optimal control of elastic joints with bounded input. manuscript accepted for publication," in *Proc. IEEE Conf. Decis. Control*, 2020, pp. 4149–4156.
[9] S. Haddadin, F. Huber, and A. Albu-Schäffer, "Optimal control for exploiting the natural dynamics of variable stiffness robots," in *Proc. IEEE Int. Conf. Robot. Automat.*, 2012, pp. 3347–3354.
[10] D. Braun, M. Howard, and S. Vijayakumar, "Optimal variable stiffness control: Formulation and application to explosive movement tasks," *Auton. Robots*, vol. 33, no. 3, pp. 237–253, 2012.
[11] D. J. Braun *et al.*, "Robots driven by compliant actuators: Optimal control under actuation constraints," *IEEE Trans. Robot.*, vol. 29, no. 5, pp. 1085–1101, Oct. 2013.
[12] N. Mansfeld, M. Hamad, M. Becker, A. G. Marin, and S. Haddadin, "Safety map: A unified representation for biomechanics impact data and robot instantaneous dynamic properties," *IEEE Robot. Automat. Lett.*, vol. 3, no. 3, pp. 1880–1887, Jul. 2018.
[13] M. Spong, "Modeling and control of elastic joint robots," *J. Dynamic Syst., Meas. Control*, vol. 109, pp. 310–318, Dec. 1987, doi: 10.1115/1.3143860.
[14] S. Wolf and G. Hirzinger, "A new variable stiffness design: Matching requirements of the next robot generation," in *Proc. IEEE Int. Conf. Robot. Automat.*, 2008, pp. 1741–1746.
[15] P. Chiacchio, Y. Bouffard-Vercelli, and F. Pierrot, "Force polytope and force ellipsoid for redundant manipulators," *J. Robot. Syst.*, vol. 14, no. 8, pp. 613–620, 1997.
[16] M. Cyrus and J. Beck, "Generalized two-and three-dimensional clipping," *Comput. Graph.*, vol. 3, no. 1, pp. 23–28, 1978.
[17] S. Haddadin, M. Weis, S. Wolf, and A. Albu-Schäffer, "Optimal control for maximizing link velocity of robotic variable stiffness joints," *World Congr. Int. Federation Autom. Control*, vol. 44, no. 1, pp. 6863–6871, 2011.
[18] S. Haddadin *et al.*, "Intrinsically elastic robots: The key to human like performance," in *Proc. IEEE/RSJ Int. Conf. Intell. Robots Syst.*, 2012, pp. 4270–4271.
[19] M. A. Patterson and A. V. Rao, "GPOPS-II: A matlab software for solving multiple-phase optimal control problems using hp-adaptive gaussian quadrature collocation methods and sparse nonlinear programming," *ACM Trans. Math. Softw.*, vol. 41, no. 1, pp. 1–37, 2014.
[20] M. Grebenstein *et al.*, "The DLR hand arm system," in *Proc. IEEE Int. Conf. Robot. Automat.*, 2011, pp. 3175–3182.
[21] O. Khatib, "Inertial properties in robotic manipulation: An object-level framework," *Int. J. Robot. Res.*, vol. 14, no. 1, pp. 19–36, 1995.
[22] A. Bicchi and G. Tonietti, "Fast and soft arm tactics: Dealing with the safety-performance trade-off in robot arms design and control," *IEEE Robot. Automat. Mag.*, vol. 11, no. 2, pp. 22–33, Jun. 2004.
[23] S. Haddadin, A. Albu-Schäffer, O. Eiberger, and G. Hirzinger, "New insights concerning intrinsic joint elasticity for safety," in *Proc. IEEE/RSJ Int. Conf. Intell. Robots Syst.*, 2010, pp. 2181–2187.
[24] T. E. Lobdell, C. K. Kroell, D. C. Schneider, W. E. Hering, and A. M. N. M. D., "Impact response of the human thorax," in *Human impact response*, Springer, pp. 201–245, 1973.
[25] S. Haddadin, A. Albu-Schäffer, and G. Hirzinger, "Requirements for safe robots: Measurements, analysis & new insights," *Int. J. Robot. Res.*, vol. 28, no. 11-12, pp. 1507–1527, 2009.